

PAPER • OPEN ACCESS

Modelling of energetic particle drive and damping effects on TAEs in AUG experiment with ECCD

To cite this article: R. Calado *et al* 2024 *Nucl. Fusion* **64** 016039

View the [article online](#) for updates and enhancements.

You may also like

- [Fast particle destabilization of toroidal Alfvén eigenmodes](#)
C.Z. Cheng, N.N. Gorelenkov and C.T. Hsu
- [Investigation of high-n TAE modes excited by minority-ion cyclotron heating in JT-60U](#)
M Saigusa, H Kimura, S Moriyama et al.
- [The effects of electron cyclotron heating and current drive on toroidal Alfvén eigenmodes in tokamak plasmas](#)
S E Sharapov, M Garcia-Munoz, M A Van Zeeland et al.

Modelling of energetic particle drive and damping effects on TAEs in AUG experiment with ECCD

R. Calado^{1,*}, F. Nabais¹, S.E. Sharapov², P. Schneider³, Ye. Kazakov⁴,
M. Garcia-Muñoz⁵, A. Snicker⁶, J. Ferreira¹, R. Coelho¹, M. Dreval⁷, J. Fuertes⁸,
J. Galdon-Quiroga³, J. Gonzalez-Martin⁹, A. Karpushov¹⁰, J. Stober³, G. Tardini³,
M.A. Van Zeeland¹¹ and the ASDEX Upgrade Team^a

¹ Instituto de Plasmas e Fusão Nuclear, Instituto Superior Técnico, Universidade de Lisboa, 1049-001 Lisboa, Portugal

² UKAEA, Culham Science Centre, Abingdon OX14 3DB, United Kingdom of Great Britain and Northern Ireland

³ Max-Planck-Institut für Plasmaphysik, Boltzmannstr. 2, 85748 Garching, Germany

⁴ Laboratory for Plasma Physics, LPP-ERM/ KMS, TEC Partner, Brussels, Belgium

⁵ FAMN Department, Faculty of Physics, University of Seville, Avda. Reina Mercedes, 41012 Seville, Spain

⁶ Department of Applied Physics, Aalto University, PO Box 14100, 00076 AALTO, Espoo, Finland

⁷ Institute of Plasma Physics, National Science Center, Kharkov Institute of Physics and Technology, 61108 Kharkov, Ukraine

⁸ Barcelona Supercomputing Center, 08034 Barcelona, Spain

⁹ Department of Mechanical Engineering and Manufacturing, University of Seville, Camino de Los Descubrimientos s/n, 41092 Seville, Spain

¹⁰ Ecole Polytechnique Fédérale de Lausanne (EPFL), Swiss Plasma Center (SPC), CH-1015 Lausanne, Switzerland

¹¹ General Atomics, PO Box 85608, San Diego, CA, United States of America

E-mail: rui.p.calado@tecnico.ulisboa.pt

Received 9 August 2023, revised 23 October 2023

Accepted for publication 16 November 2023

Published 12 December 2023



Abstract

The impact of electron cyclotron current drive (ECCD)-driven current on toroidicity-induced Alfvén eigenmodes (TAEs) in experiments on the AUG tokamak is investigated numerically. The dynamical evolution of the plasma profiles and equilibria are modelled with European transport solver, while ion cyclotron resonance heating-accelerated H-minority ions exciting TAEs are assessed with the PION code. TAEs, their drive and damping are computed with the codes CASTOR and CASTOR-K. In the set of discharges analysed, two groups of TAEs are observed, differing in frequency and radial location. Experimental observations show that when counter-ECCD is applied the higher frequency group of approximately 150 kHz is suppressed, while the lower frequency modes of 125 kHz are amplified. When co-ECCD is applied,

^a See Stroth *et al* 2022 (<https://doi.org/10.1088/1741-4326/ac207f>) for the ASDEX Upgrade Team.

* Author to whom any correspondence should be addressed.



Original Content from this work may be used under the terms of the [Creative Commons Attribution 4.0 licence](https://creativecommons.org/licenses/by/4.0/). Any further distribution of this work must maintain attribution to the author(s) and the title of the work, journal citation and DOI.

depending on the location of the ECCD current deposition layer, both groups of TAE can be suppressed. Numerical calculations of energetic particle drive and thermal plasma damping show that neither one effect could explain the variety of the experimental observations. The fine balance between the drive, sensitive to the TAE position, and the radiative and continuum damping effects could only explain the experiment if the effects are considered all together.

Keywords: tokamaks, Alfvén eigenmodes, energetic ions, ECCD

(Some figures may appear in colour only in the online journal)

1. Introduction

Supra thermal or energetic ion populations can resonantly excite Alfvén waves in magnetic confinement fusion devices [1, 2]. Those Alfvén instabilities may grow to high amplitudes and result in a significant increase of the cross-field transport of the energetic ions, thus causing radial redistribution and losses of the ions to the first wall. In future fusion reactors, the most important of such populations will be fusion-born alpha-particles and populations accelerated by auxiliary plasma heating mechanisms such as neutral beam injection (NBI) and ion cyclotron resonance heating (ICRH) [3]. Alpha populations and auxiliary heating populations typically have distributions peaked in the plasma core where they are needed to keep the plasma burning. When wave-particle interaction leads to substantial redistribution of core energy to outer regions of the plasma, the temperature at the core may drop below the requirements for sustained operation of the reactor.

Due to the existence of radial gradients in the plasma density and the magnetic field, the dispersion relation of the shear Alfvén wave is a function of the radius. The shear Alfvén spectrum then forms a continuum. Modes in the continuum range of frequency are hard to excite due to a process known as continuum damping [4, 5]. There are, however, geometric effects that introduce gaps in the Alfvén continuum. Inside these gaps, a discrete spectrum of eigenmodes can exist, which are much easier to excite given the absence of continuum damping. An important example of such modes are the Toroidicity-induced Alfvén Eigenmodes (TAEs) [6, 7], which reside in gaps created by toroidicity effects. These modes can resonantly interact with energetic ion populations and redistribute these energetic ions to outer plasma regions, possibly leading to ion losses [8, 9].

It is important to develop methods to mitigate Alfvén instabilities in order to avoid core energy redistribution and prevent the loss of energetic ions, which would collide with and damage reactor walls and other plasma facing components. Drive from energetic ions competes against a variety of damping effects. To mitigate instabilities, one should search for mechanisms that either decrease the drive or increase the damping of the wave (or both), or that suppress entirely the existence of the discrete spectrum. One way to control operational conditions is by applying electron cyclotron resonant heating (ECRH) that locally affects the plasma pressure and density profiles [10].

Methods to control Alfvénic activities using ECRH and ECCD (electron cyclotron current drive) are being developed in AUG [11–13]. In a set of recent discharges employing ECCD, distinct TAE groups were observed to be suppressed when different ECCD configurations were applied [14]. A reference discharge was performed with ECRH so that no current was driven. In this discharge, a higher frequency and a lower frequency groups of TAEs were observed. The frequencies of the first group are close to 150 kHz, and the second group is characterised by frequencies around 125 kHz. In following discharges, ECCD was configured to drive current either opposite to or in the same direction as the plasma current. In the former scenario, only the low frequency TAEs are observed, whereas in the latter, only the high frequency modes were unstable. ECCD has a localised effect on the current profile and subsequently on the continuum spectrum, thereby possibly closing continuum gaps and modifying the position and frequency of the modes. These effects impact TAEs' drive and damping mechanisms and may ultimately result in suppression of the modes. In this work, the set of discharges is analysed in order to understand the mitigation of the observed modes and to establish a connection to the applied ECCD schemes.

The paper is organised as follows. In section 2, the experiments are described and the observations that led to the work are presented. The ensuing modelling work is presented in section 3, with three discharges being analysed in detail. The results obtained are discussed and conclusions are drawn in section 4.

2. Experimental observations

In order to study the effects of ECCD on the TAEs, three different scenarios were devised. The first scenario is an ECRH scenario with no ECCD driven current. It was thus a reference scenario where the TAE activity in the absence of ECCD effects was identified. This scenario was explored in discharge No 38012. After that, the following discharges were performed with two different ECCD configurations. In discharge No 38017, ECCD was configured to generate current in the opposite direction of the plasma current. In contrast, in discharge No 38019 ECCD generated current in the same direction as the plasma current. In this manuscript, we refer to these configurations as counter-ECCD and co-ECCD, respectively. The ECCD channels were tuned to generate current at different radial locations. The channels were successively turned on in a step fashion in order to identify the ECCD power threshold

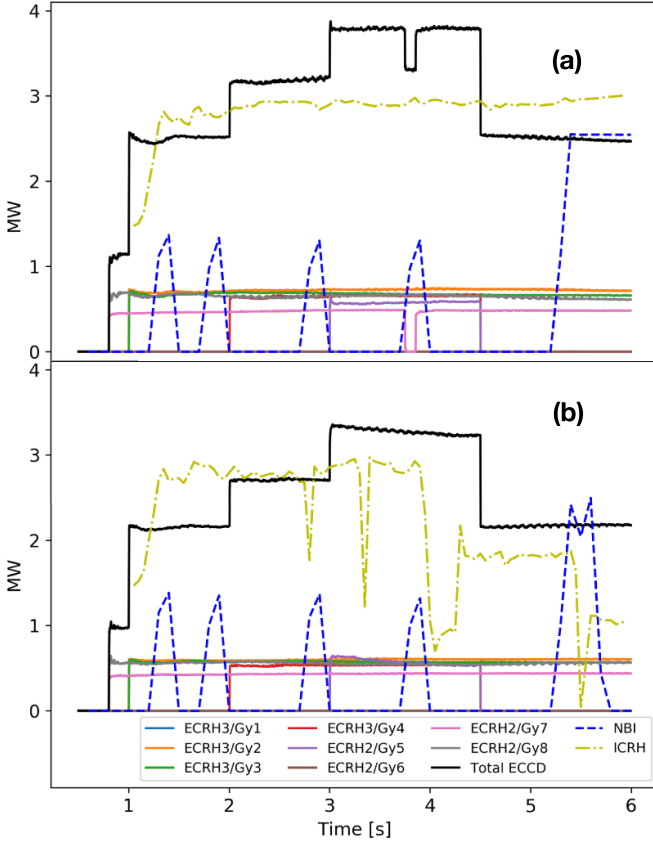


Figure 1. Power waveforms of the different ECCD channels, ICRH and NBI from discharges No. (a) 38017; (b) 38019.

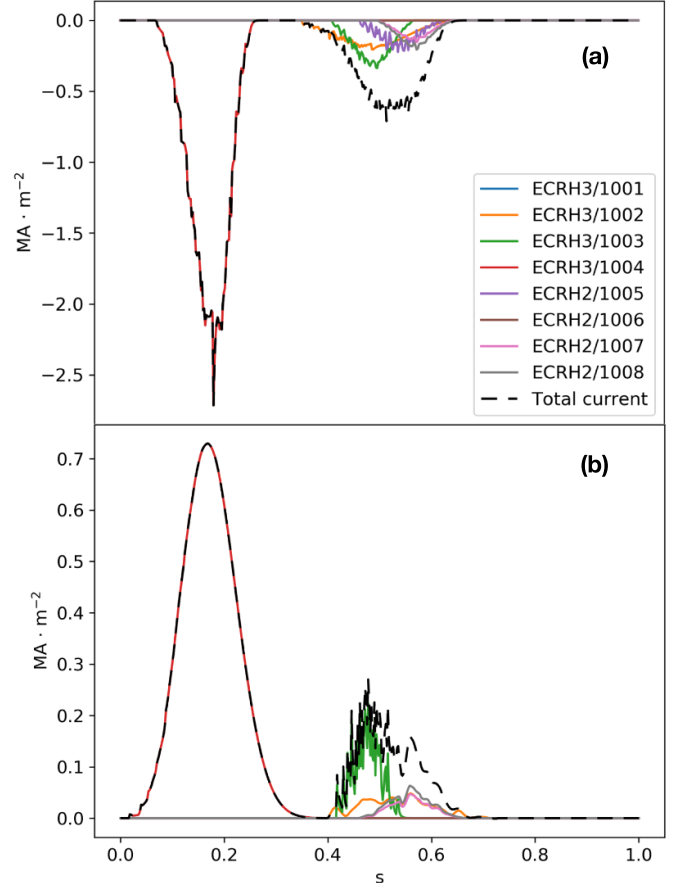


Figure 2. ECCD current deposition profile of: (a) discharge 38017 at $t = 3.6$ s; (b) discharge 38019 at $t = 2.25$ s.

for mode suppression and investigate the effect of current generation at different locations. The power waveforms of the different ECCD channels, ICRH and NBI during the counter-ECCD and co-ECCD discharges are shown in figure 1. NBI was injected tangentially in blips for diagnostics purposes. The current deposition profiles from the different channels in both discharges are shown in figure 2. They are shown as a function of the square root of the normalised poloidal flux, $s = \sqrt{\Psi_{\text{norm}}}$. The negative sign of the current in discharge 38017 represents the opposite direction of the driven current relative to the plasma current. In both scenarios, channel 4 has the strongest effect on the current and has a deposition profile peaked around $s \approx 0.2$. The effect from other channels is farther from the axis in the $s = 0.4$ – 0.6 range.

Figure 3 shows spectrograms in the TAE range of frequencies corresponding to discharges No (a) 38012, (b) 38017 and (c) 38019. In the reference discharge both lower (120–130 kHz) and higher (140–150 kHz) frequency TAEs were observed in the interval $t = 1.75$ – 3.5 s. Multi-coil analysis allows the identification of the toroidal mode numbers of the lower frequency modes as $n = 2, 3$ while the higher frequency mode has $n = 2$. Additional signals observed in the spectrograms represent the result of the interference of the high frequency $n = 2$ mode and the harmonics of an $n = 1$ Neoclassical Tearing Mode (NTM). The radial localisation of the TAE modes was estimated using ECE data. The higher frequency

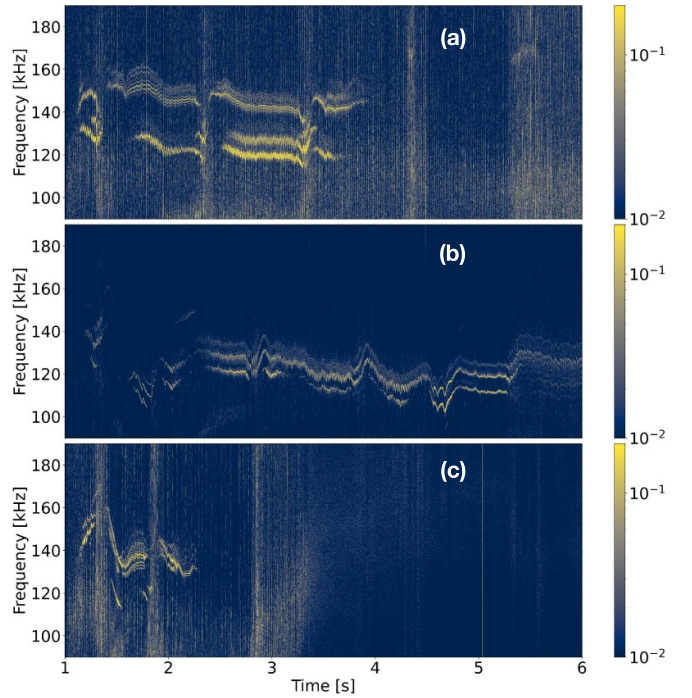


Figure 3. Spectrograms of discharges No. (a) 38012; (b) 38017; (c) 38019.

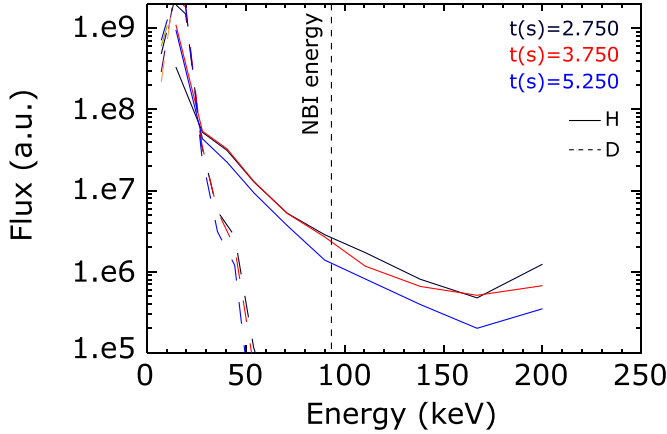


Figure 4. NPA measurements of H and D ions during discharge 38017.

modes were found to reside near $s=0.4$, and the lower frequency modes were localised close to $s=0.6$, where s is the square root of the normalised poloidal flux. When counter-ECCD was applied to the plasma, only modes in the lower frequency range were observed, as figure 3(b) shows. The observed modes have toroidal mode numbers $n=2, 3, 4$ during the interval $t=2.5$ – 4 s, after which the $n=2$ becomes stable and an $n=5$ mode emerges. They are localised close to the $s=0.6$ surface. Frequency range, mode localisation and toroidal mode numbers agree with the observations for the lower frequency modes of the reference discharge. In the co-ECCD discharge only modes in the higher frequency range are observed throughout the discharge up until shortly after $t=2$ s. Toroidal mode analysis shows that these modes are characterised by $n=2, 3$. The other signals observed in figure 3(c) are once again the result of the beating of the $n=2$ and $n=3$ TAEs with the harmonics of an $n=1$ NTM. ECE diagnostics localise the TAE modes between $s=0.4$ and $s=0.6$.

The modes were excited by an ICRH accelerated H minority population. Evidence of this population was collected by NPA measurements as shown in figure 4 for discharge 38017.

3. Modelling

Numerical modelling was employed to understand the suppression of the TAEs in the different ECCD scenarios. With this purpose in mind, drive from the energetic ions population and damping from relevant damping mechanisms were calculated. The time evolving equilibria of the discharges were computed with European transport solver (ETS) [15, 16] and the straight field line coordinate system representation for these equilibria was obtained with HELENA [17]. Alfvén continuum and eigenmode calculations were carried out with the resistive MHD codes CSCAS [18] and CASTOR [19], respectively, to identify the modes observed in the spectrograms. Drive from the ICRH excited fast H population as well as Landau damping from the bulk D plasma was then assessed

for each mode with CASTOR-K [20]. In this code, each ion species is described by a distribution function in the (E, s, Λ) phase space, assumed to be factorable as

$$f(E, s, \Lambda) = n(s)f_E(E)f_\Lambda(\Lambda),$$

which the code converts to the equivalent distribution in the phase space of the constants of motion (E, P_ϕ, Λ) , where $E, P_\phi \equiv Ze\Phi + mRv_\parallel B_\phi/B$ and $\Lambda \equiv \mu B_0/E$ are the particle's energy, toroidal canonical momentum and normalised magnetic moment, respectively. It was assumed for both species that f_E is described by a Maxwellian distribution, where for the radial temperature profile $T(s)$ an 8th order polynomial was considered. The density profile $n(s)$ was also described by an 8th order polynomial in the case of the fast H population, whereas in the case of the bulk D population the density profile was taken to be in the form:

$$n(s) = [c_1 + s(c_2 + s(c_3 + c_4s))] \cdot [1 - \tanh((s - c_5)/c_6)].$$

Fast H density and temperature radial profiles were fitted to data from PION [21] runs, and the bulk D profiles were fitted to ETS data. As for f_Λ , a boxcar function was used, where $f_\Lambda(\Lambda)$ is constant in a given Λ range and 0 elsewhere. The bulk D ions were assumed to be distributed isotropically. Since ICRH was configured for on-axis heating of the H population, Λ ranges close to unity were considered for this population. Figure 5 illustrates the procedure to identify the best suiting range for Λ . From the figure, it is clear that depending on the value of Λ considered the population provides drive (positive γ) or damping (negative γ) to the mode. A wide range is first considered, from which the Λ interval that matches the requirements in terms of drive for both modes is selected. The example shown here corresponds to the counter-ECCD discharge, where drive of the low frequency mode should be stronger than damping, and the opposite for the high frequency mode. The interval selected maximizes drive of the low frequency mode while constraining the high frequency mode to medium drive. Moving the interval to minimize the high frequency mode drive would also decrease drive of the low frequency mode, which is not desirable as the mode should have a positive net growth rate. A note should also be made on fast H drive and Landau damping calculations when the modes intersect the continuum at locations where mode amplitude is significant. That is the case of the low frequency modes observed in the experiments. To avoid spurious energy exchange contributions arising from the sharp singular behaviour of the eigenfunction where crossing the Alfvén continuum, a radial range restricted version of the eigenfunction was considered in CASTOR-K calculations.

Aside from ion Landau damping, two additional sources of damping were also considered: continuum damping and radiative damping. Both continuum and radiative damping were computed with CASTOR. Continuum damping was computed based on the results of [5]. Resistivity (η) scans on the vanishing resistivity limit $\eta \rightarrow 0$ show the oscillatory and damping parts of the resistive MHD eigenmode converging to finite,

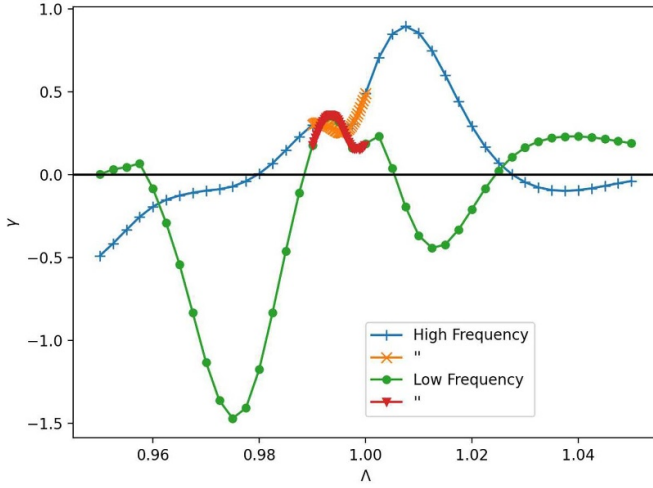


Figure 5. Growth rate γ dependence on Λ of the fast H ions. From the wide range calculations (blue crosses and green circles for the high and low frequency modes, respectively) the best suiting interval is selected, here $\Lambda = [0.99; 1.00]$ (orange Xs and red triangles for the high and low frequency modes, respectively).

η independent values as η decreases. The damping obtained in this limit corresponds to the continuum damping due to coupling to ideal MHD continuum modes. Radiative damping, on the other hand, comes from coupling of the TAEs to kinetic Alfvén waves (KAWs). These waves propagate in the radial direction and carry energy away from the TAE, effectively damping it. Comprehensive descriptions of the approach followed to estimate radiative damping can be found in [22, 23]. It is based on the formal equivalence between a non-ideal MHD model accounting for finite parallel electric field and first-order ion gyroradius effects, which give rise to KAWs, and the resistive MHD model of CASTOR, if η is extended to the complex plane. The imaginary part of η introduces coupling to KAWs, while the real part is connected to collisional damping, an effect much stronger for KAWs than for TAEs. From scans performed on the real part of η it is possible to identify the point where all KAW energy is damped, providing an estimation for the radiative damping of the TAE.

3.1. Reference ECRH—discharge 38012

Figure 6 exhibits the spectrogram and the ECRH, NBI and ICRH power waveforms of discharge 38012. ECRH channels during the interval $t = 1.0$ – 3.5 s were configured to have no effect on the current. However, channel 4 was not correctly configured and at $t = 3.5$ s, when it was turned on, it started driving significant current opposite to the plasma current. Shortly after the modes were suppressed. Thus, the reference discharge was considered only until $t = 3.5$ s in our analysis.

During the time interval under consideration, the q profile of the equilibrium was monotonic. Figure 7 shows the q profile at $t = 3.41$ s and the $n = 2$ and $n = 3$ Alfvén continua computed with CSCAS at the same instant. ECE analysis located the higher and lower frequency $n = 2$ modes at $s \approx 0.4$ and

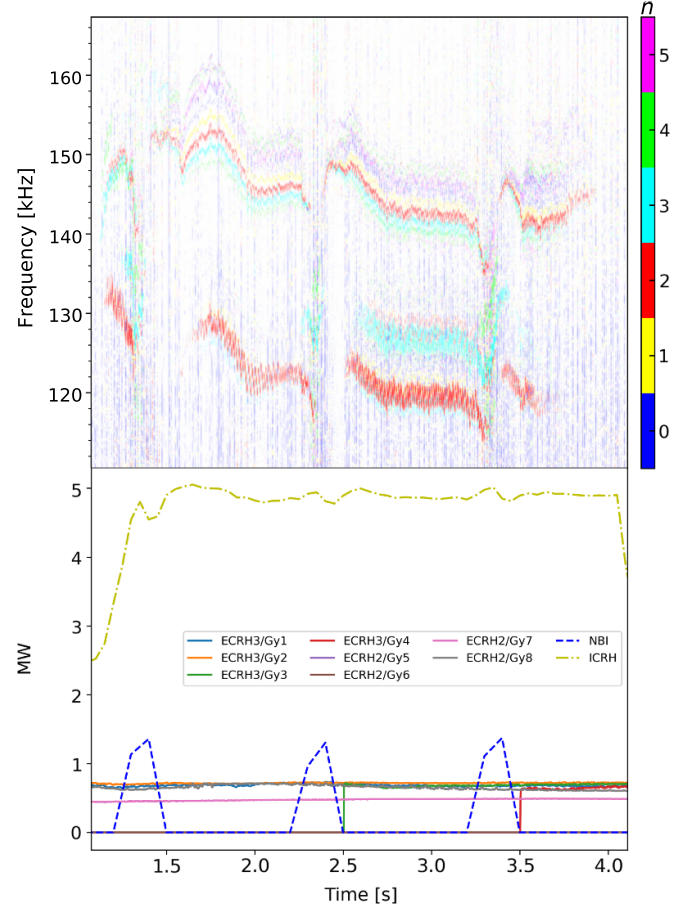


Figure 6. Spectrogram (top) and ECRH (solid), NBI (dashed) and ICRH (dash-dotted) power waveforms (bottom) from the reference discharge. NBI has a strong effect on the observed frequency of the modes. Shortly after ECRH channel 4 (red solid curve) is accidentally turned on at $t = 3.5$ s the modes are suppressed.

$s \approx 0.6$, respectively. From figure 7 one can observe that these locations correspond to local extrema of the Alfvén continuum where a gap is formed.

Frequencies corresponding to the bottom of the gaps at $s \approx \{0.4; 0.6\}$ were scanned for TAEs with CASTOR. A mode was found at each gap. The computed radial structures and frequencies are shown in figure 8. To the frequencies computed by CASTOR a Doppler shift of $\Delta f = n \times 6$ kHz is added to take into account plasma rotation. The 6 kHz plasma rotation frequency was estimated from the frequency separation observed between the $n = 2$ and $n = 3$ modes observed in the low frequency range. The frequencies thus obtained (137 kHz and 106 kHz) are lower than those observed in the experiments (145 kHz and 121 kHz), especially for the lower frequency mode, whereas the position of the modes is in good agreement with ECE measurements. The higher frequency mode only intersects the continuum at a location where its amplitude is low, and as such this mode is not expected to suffer significant continuum damping. As for the lower frequency mode, there is an intersection with the continuum at a location where the mode's amplitude is still significant. The mode was, however, clearly observed in the experiments, indicating that continuum

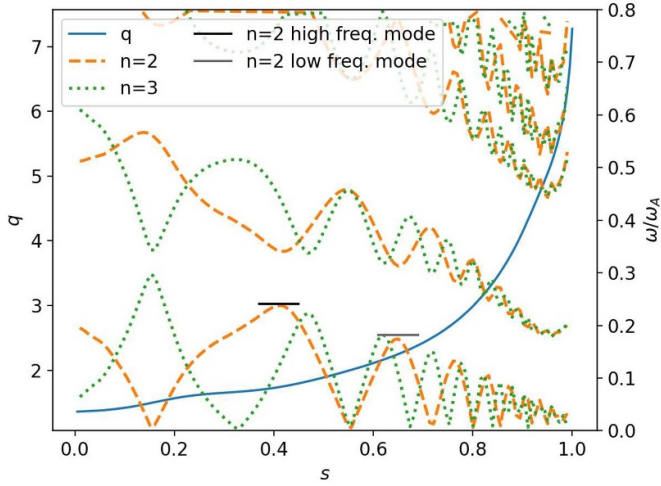


Figure 7. q profile (solid blue) and the $n = 2$ (orange dashed) and $n = 3$ (green dotted) Alfvén continua of the reference discharge 38012 at $t = 3.41$ s, before ECCD channel 4 is active. The $n = 2$ higher and lower frequency modes sit at the two leftmost continuum gaps. The location of these gaps matches the location of the observed modes. The frequencies of the TAEs found at the bottom of these gaps by CASTOR are marked by the horizontal black and grey lines.

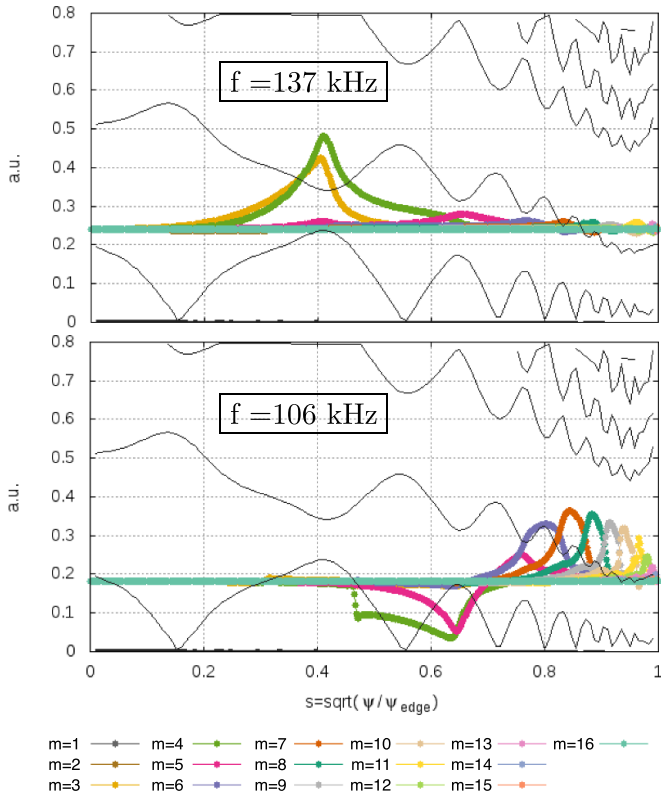


Figure 8. $n = 2$ Alfvén continuum and eigenmodes obtained with CASTOR in discharge 38012 at $t = 3.41$ s.

damping should not be enough to overrule the fast H population drive.

The effects of the different drive and damping mechanisms were computed for the modes displayed in figure 8. The

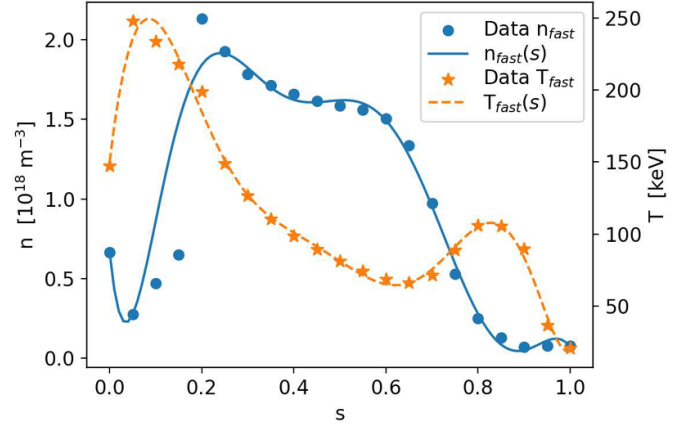


Figure 9. Density and temperature profiles of the fast H population in discharge 38012 at $t = 3.41$ s. Data points are obtained with PION and the lines represent the fitted $n_{\text{fast}}(s)$ and $T_{\text{fast}}(s)$ that are introduced in CASTOR-k.

Table 1. Drive and damping results at $t = 3.41$ s for the higher and lower frequency $n = 2$ modes presented in figure 8.

Mode	γ/ω (%)			
	Fast H	Bulk D	Radiative	Continuum
High f	9.24	−0.55	−2.45	−0.01
Low f	4.10	−0.98	−1.99	−0.67

fast H temperature and density radial profiles obtained with PION are shown in figure 9. The Λ range considered was $\Lambda = [1.00; 1.01]$. These profiles were used in the calculation of the drive from the fast H population. Data from ETS was fitted and yielded the profiles for the bulk D plasma distribution that were assumed for the Landau damping calculations. The drive and damping results are presented in table 1.

The results shown in table 1 agree with the experimental observations. Both modes experience sufficient drive from the interaction with the fast H population to sustain the combined effects of Landau, radiative and continuum damping. Additionally, the high frequency mode does not experience strong continuum damping. The low frequency mode, on the other hand, intersects the continuum at a location where its amplitude is significant, and the corresponding continuum damping is stronger.

3.2. Counter-ECCD—discharge 38017

In figure 10 the spectrogram of discharge 38017 is shown, together with the power waveforms of ECCD and NBI. ECCD is applied from the beginning, with the most significant channel in terms of current drive (channel 4) being active during the interval $t = 2.0$ – 4.5 s. Modes in the lower frequency range are present throughout the discharge, while the higher frequency modes observed in the reference discharge are here suppressed from the start. When ECCD channel 4 is powered, the modes seem to be amplified.

Due to the current driven by channel 4 exhibiting a strongly peaked deposition profile around $s = 0.2$, the q profile during

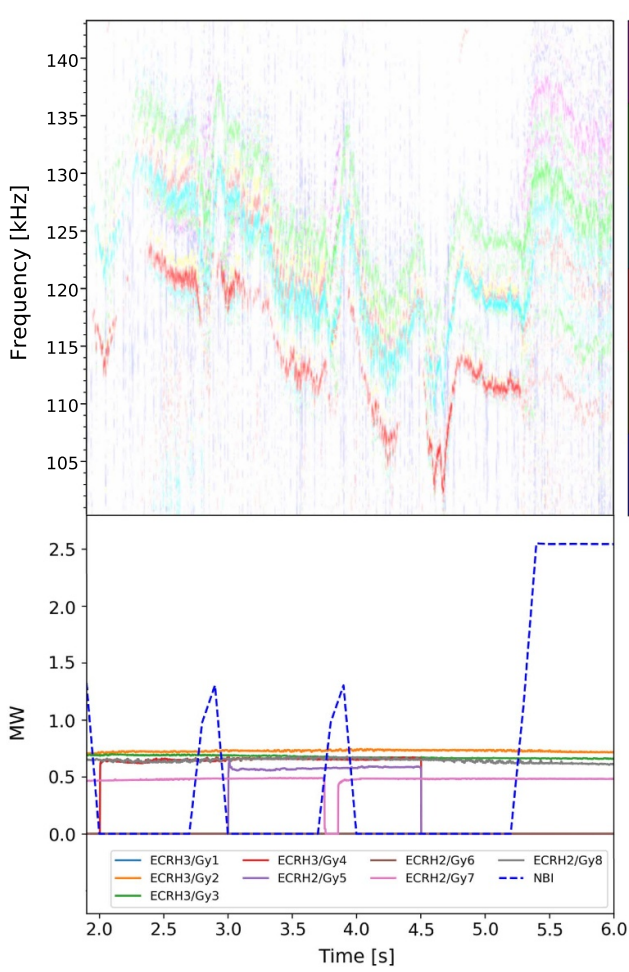


Figure 10. Spectrogram (top) and ECCD (solid) and NBI (dashed) power waveforms (bottom) from the counter-ECCD discharge. NBI effects are reflected by the changes in the observed frequency of the modes. The lower frequency modes are visible throughout the discharge while different channels are being turned on and off.

the period of activity of this channel was no longer monotonic. The continuum structure is consequently severely affected. Figure 11 illustrates the effect of ECCD on both q and the Alfvén continuum structure. A prominent bump arises in the q profile close to the current deposition location of channel 4. The elevated magnetic shear on the inner side of the bump results in a rapid change of the frequency of the continuum around $s = 0.2$, closing the TAE gap at this location. At higher minor radius, q decreases more slowly and the subsequent shear reversal is smoother. There is a local minimum of q around $s = 0.3$. The current generated by the other ECCD channels is localised in the $s = 0.5$ – 0.6 region. The effect of this current on q is also observed in figure 11 in the local increase of the magnetic shear. However, the current is not enough to reverse the shear as in the case of channel 4. The subsequent effect on the Alfvén continuum structure is the inwards displacement of the gap seen in the reference discharge slightly after $s = 0.6$.

Once again, frequencies at the bottom of the gaps at $s \approx 0.5$ – 0.6 were numerically scanned for $n = 2$ TAEs. The scans yielded modes centred at each of these locations, shown in figure 12. We conclude from this result that the absence

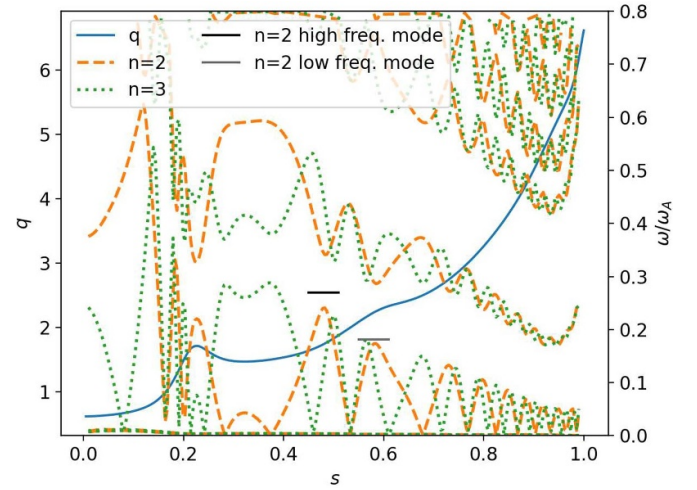


Figure 11. q profile (solid blue) and the $n = 2$ (orange dashed) and $n = 3$ (green dotted) Alfvén continua of the counter-ECCD discharge 38017 at $t = 3.60$ s. The continuum gaps at $s \approx 0.6$ match the location and frequency of the experimentally observed modes. At $s \approx 0.5$ sits another gap corresponding to the leftmost gap of the reference discharge, where the higher frequency mode was found. At each of these gaps a TAE was found, marked here with black and grey horizontal lines.

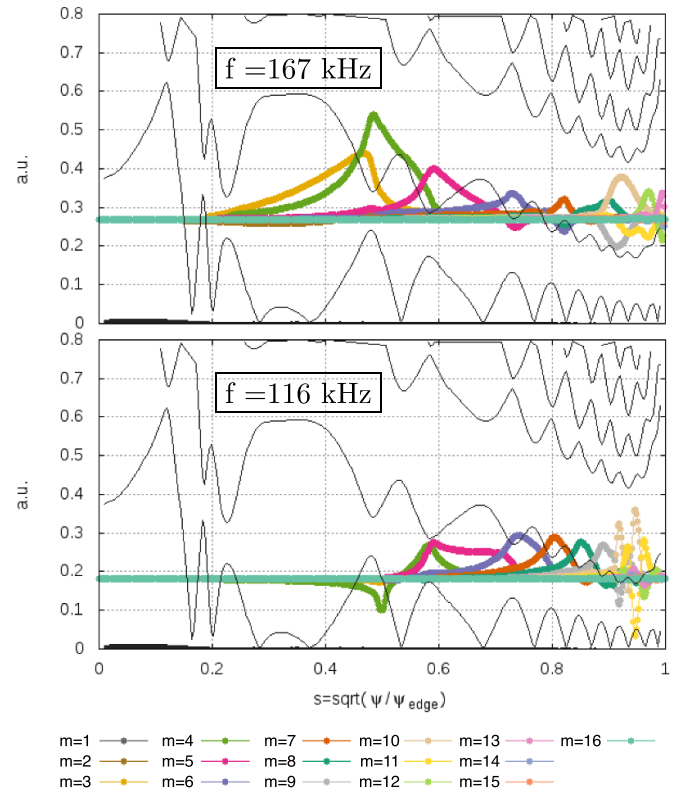


Figure 12. $n = 2$ Alfvén continuum and eigenmodes obtained with CASTOR in discharge 38017 at $t = 3.60$ s.

of higher frequency modes in discharge 38017 is not due to continuum changes that disallow the existence of gap modes, but rather to the increase/decrease of damping/drive. In this discharge, a plasma rotation frequency of 7 kHz was considered in the calculation of the Doppler shift to the

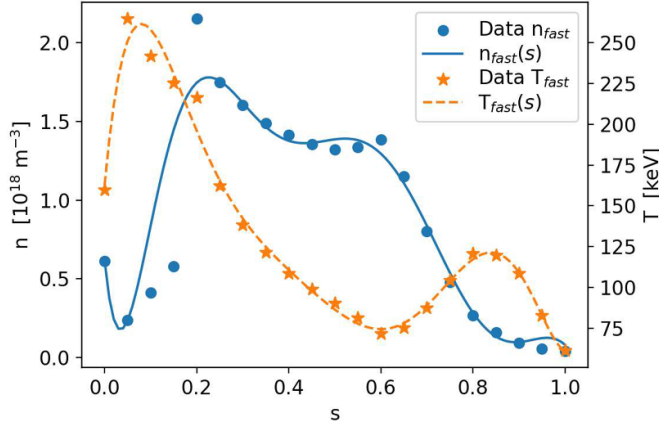


Figure 13. Density and temperature profiles of the fast H population in discharge 38017 at $t = 3.60$ s. Data points are obtained with PION and the lines represent the fitted $n_{\text{fast}}(s)$ and $T_{\text{fast}}(s)$ that are introduced in CASTOR-k.

Table 2. Drive and damping results at $t = 3.60$ s for the higher and lower frequency $n = 2$ modes presented in figure 12.

Mode	γ/ω (%)			
	Fast H	Bulk D	Radiative	Continuum
High f	5.84	−0.05	−3.45	−0.17
Low f	4.82	−0.21	−0.96	−2.5

frequencies computed with CASTOR. The frequency and location of the TAE at the $s \approx 0.6$ gap match those of the experimentally observed $n = 2$ mode. At the location of the intersection of the mode with the continuum the mode's amplitude is significant. The mode found at the $s \approx 0.5$ gap has a higher frequency than that of the higher frequency modes observed in the reference discharge. The case differs from the reference scenario in that this mode intersects the continuum both at the core and at outer regions, however at both locations the amplitude of the mode is low.

Drive and damping mechanisms were evaluated for both modes. The density and temperature profiles of the fast H population used in the calculations were obtained with PION and are shown in figure 13. They are very similar in shape to the profiles in the reference case, but with slightly lower density and slightly higher temperature. The Λ range considered for this species was in this case $\Lambda = [0.99; 1.00]$. The results are shown in table 2.

In this discharge, the unstable nature of the low frequency mode is compatible with drive and damping estimations, as the computed drive from the fast H population is stronger than the combined effect of the damping sources. However, our calculations do not explain the suppression of the high frequency mode. It was expected that the high frequency mode experiences in this discharge stronger continuum damping since in this scenario the mode intersects the continuum at an additional location around $s \approx 0.2$. This in fact agrees with our calculations. However, this effect, even combined with a decrease

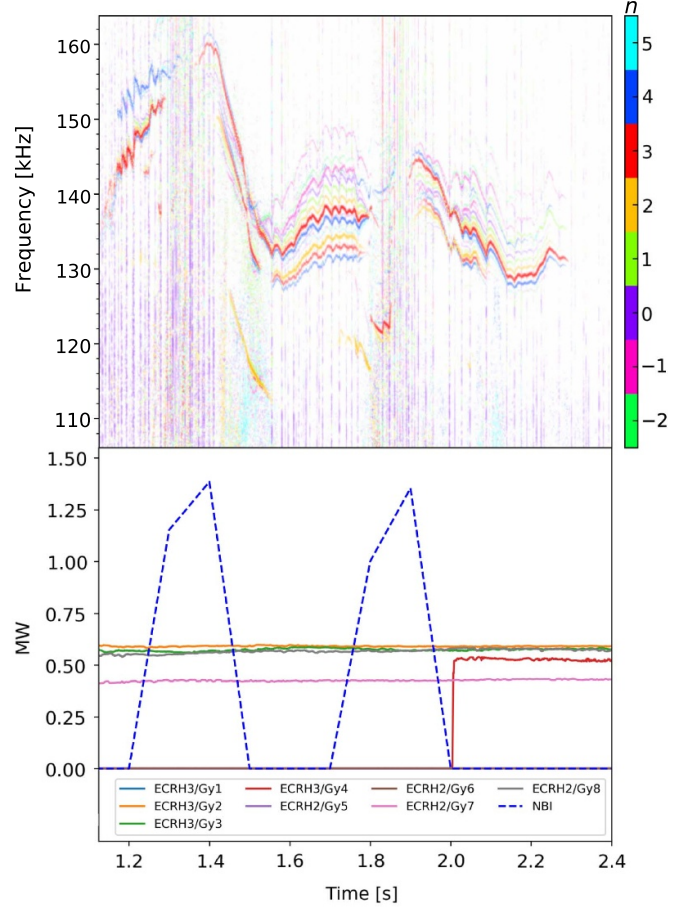


Figure 14. Spectrogram (top) and ECCD (solid) and NBI (dashed) power waveforms (bottom) from the co-ECCD discharge. The higher frequency modes are present until shortly after $t = 2$ s, when ECCD channel 4 is turned on. From $t \approx 1.5$ s onwards, two groups of modes are observed. The lower and higher frequency groups are dominated by the $n = 2$ and $n = 3$ mode, respectively, with the neighbouring modes resulting from beatings with an NTM and its harmonics.

in fast H drive and increase in radiative damping, was not enough to obtain net mode damping.

3.3. Co-ECCD—discharge 38019

The spectrogram and the power waveforms of ECCD and NBI of discharge 38019 are shown in figure 14. It is only shortly after channel 4 is turned on that the higher frequency modes are suppressed. This observation suggests that the current deposition location impacts the suppression of the modes. As for the lower frequency modes, they are suppressed throughout except for very brief periods.

Opposite to the counter-ECCD discharge, the driven current increased the plasma current locally around $s = 0.2$. The increase in current leads to a decrease in the local q value. When ECCD channel 4 is active, the q profile becomes non-monotonic as shown in figure 15. The figure also shows the $n = 2$ and $n = 3$ continua at $t = 2.25$ s. In agreement with ECE data localising the observed modes in the $s = 0.4$ – 0.6 region,

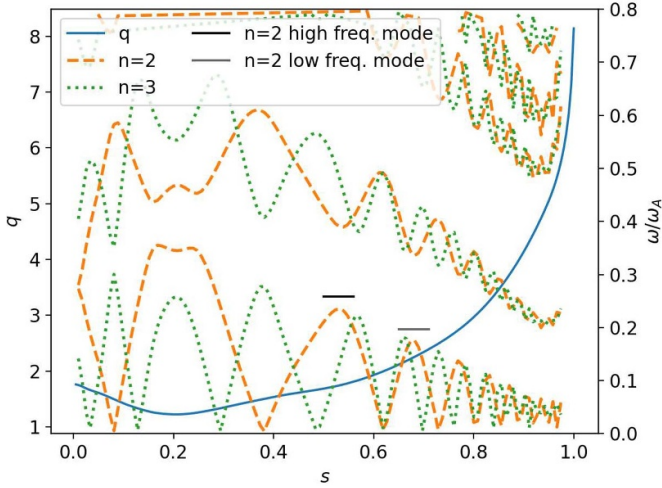


Figure 15. q profile (solid blue) and the $n = 2$ (orange dashed) and $n = 3$ (green dotted) Alfvén continua of the co-ECCD discharge 38019 at $t = 2.25$ s. The continuum gaps close to $s = 0.55$ are in good agreement in terms of frequency and location with the observed modes. At $s \approx 0.7$ a gap is found which, albeit slightly deviated outwards, corresponds to the lower frequency gap of the reference discharge. Once again, the eigenmodes found at each of these gaps are marked by the horizontal black and grey lines.

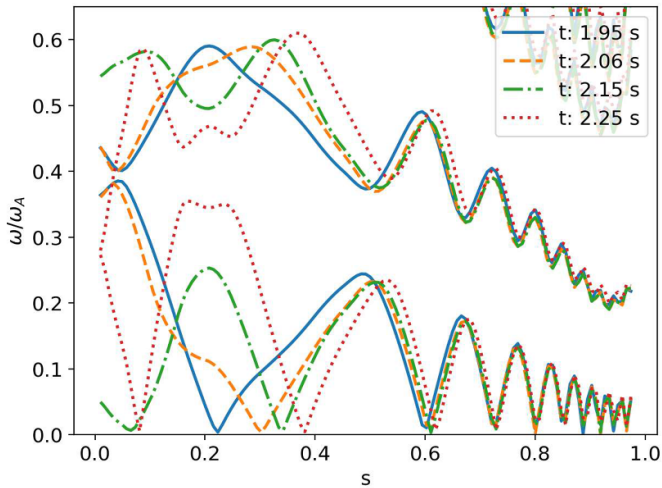


Figure 16. $n = 2$ Alfvén continuum evolution. At $t = 2.0$ s ECCD channel 4 is powered on, and its effect on the current profile is reflected on the evolution of the continuum through the safety factor. As the q profile becomes non-monotonic, at the location of its minimum, around $s = 0.2$, a bump in the continuum appears and rises, a structure associated with the RSAE. Eventually, the bump closes the TAE continuum gap from the inside.

there is a local maximum of the continuum close to $s = 0.55$. This gap corresponds to the one at $s \approx 0.4$ in the reference discharge. The direct match to the $s \approx 0.6$ gap of the reference discharge is in this discharge located close to $s = 0.7$.

Figure 16 illustrates the evolution of the $n = 2$ continuum when ECCD channel 4 is turned on, at $t = 2.0$ s. As q decreases around $s = 0.2$ and the profile becomes non-monotonic, a RSAE structure is formed. Following the decrease in q , the bump in the continuum rises until it starts closing the TAE

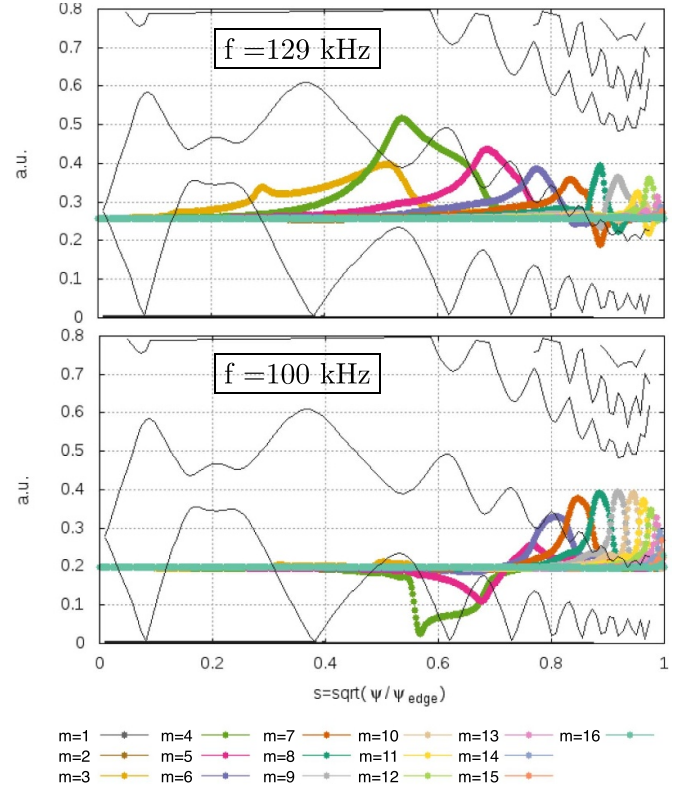


Figure 17. $n = 2$ Alfvén continuum and eigenmodes obtained with CASTOR in discharge 38019 at $t = 2.25$ s.

continuum gap from below. At $t = 2.25$ s the RSAE structure closes the lower part of the gap at the inner side.

Figure 17 shows the radial structure and frequency of the $n = 2$ modes found with CASTOR at the bottom of the gaps at $s \approx \{0.4; 0.6\}$ in the instant $t = 2.25$ s. Here, a 3 kHz frequency for the plasma rotation was assumed and hence a Doppler shift of 6 kHz was added to the computed frequency of the $n = 2$ modes. Although only one mode is observed in the experiment, a mode was found for each gap. The higher frequency mode's properties, namely frequency and radial location, match better the experimental data. Analysing the evolution of the continuum shown in figure 16 we can see that the intersection of the mode with the continuum in the inner side occurs at positions of increasing amplitude as the bump at $s \approx 0.2$ rises. Decrease of drive or increase of damping, or both, relative to the reference discharge, is expected to be behind the suppression of the lower frequency modes, since an eigenmode solution is found at this frequency range. At the intersection of this mode with the continuum its amplitude is high, which suggests strong continuum damping effects.

Figure 18 shows the density and temperature profiles of the fast H population at $t = 1.945$ s and $t = 2.25$ s. The plateau observed in the fast H density profile of the reference discharge is less pronounced in this discharge at $t = 1.95$ s, and at $t = 2.25$ s it changes to a monotonically decreasing region with much smaller slope than that observed around $s = 0.6$. The temperature profile is again similar in shape to the reference discharge but at slightly lower temperatures. In this

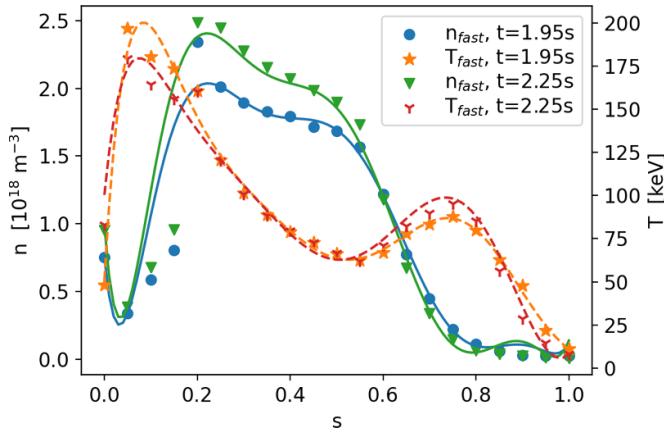


Figure 18. Density and temperature profiles of the fast H population in discharge 38019 at $t = \{1.95, 2.25\}$ s. Data points are obtained with PION and the lines represent the fitted $n_{\text{fast}}(s)$ and $T_{\text{fast}}(s)$ that are introduced in CASTOR-k.

Table 3. Drive and damping results for the higher and lower frequency $n = 2$ modes of discharge 38019 at two different times, $t = 1.95, 2.25$ s. At $t = 1.95$ s the $n = 2$ higher frequency mode is visible, but at $t = 2.25$ s it has been suppressed.

Time	Mode	γ/ω (%)			
		Fast H	Bulk D	Rad	Cont
1.95	High f	4.12	−0.05	−1.23	−0.21
	Low f	1.49	−0.23	−3.08	−1.5
2.25	High f	−1.00	−0.13	−0.94	−0.22
	Low f	1.64	−0.94	—	−1.98

discharge, the Λ intervals considered for the fast H population were $\Lambda = [1.00; 1.01]$ at $t = 1.945$ s and $\Lambda = [0.995; 1.005]$ at $t = 2.25$ s. The drive and damping results obtained are presented in table 3.

When co-ECCD was applied, a decrease of fast H drive to the low frequency mode relative to the reference discharge is observed. Additionally, radiative and continuum damping increase. Decrease of drive and increase of damping explain the suppression of the mode in this scenario. Regarding the suppression of the high frequency mode, our results suggest that it is due to decrease of the fast H drive, further enhanced after ECCD channel 4 is powered where the fast H population is expected to damp the mode according to our calculations.

4. Discussion and conclusions

An AUG experiment performed to investigate the TAE suppression effect of ECCD was analysed in this work. The goal was to understand and explain the suppression of TAEs observed in the experiment's discharges when different ECCD schemes were employed. A reference discharge with ECRH only and discharges with ECCD driving current either in the same or in the opposite direction of the plasma current where studied. In the reference discharge, where no ECCD

was applied, two groups of TAEs were observed. The $n = 2$ mode of each group was numerically computed and identified with CASTOR, with good agreement with experimental observations both in frequency and location of the mode. Similar numerical eigenmode solutions were found in the counter-ECCD and co-ECCD scenarios, suggesting mode suppression in the ECCD discharges to result from changes in the magnitude of drive and damping effects that lead to damping mechanisms exceeding the source of drive.

Mode drive due to interaction with an ICRH accelerated H minority was evaluated with CASTOR-K. The results were observed to be strongly dependent on the Λ interval of the energetic ion population. Except for the counter-ECCD case, an interval was found for the remaining discharges where the results agreed with the observations, in the sense that the drive obtained was stronger than damping sources when the corresponding mode is observed, and lower when the mode is suppressed. Changes in drive magnitude are connected with ECCD effects changing the radial position of the modes, taking them to regions of higher/lower energetic ion density and radial density gradient.

Our calculations in the counter-ECCD discharge show a decrease in the drive of the high frequency $n = 2$ TAE, as well as an increase of total damping. The mitigating effect of this counter-ECCD scheme is reflected in the decrease of the net growth rate of the mode with respect to the reference discharge. However, our calculations were unable to capture the full extent of this effect since drive was estimated to be stronger than damping even though the mode is suppressed in the discharge. Inaccuracy of equilibrium reconstructions is a source of uncertainty that may explain overestimation of the drive and/or underestimation of damping effects. Calculations for the low frequency yield a positive net growth rate, in agreement with the observation of the mode during the discharge. The computed growth rate for this mode was larger than in the reference discharge. These results support the observation that counter-ECCD has a mitigating effect on the high frequency TAEs but an enhancing effect on the low frequency TAEs. The location of the ECCD current deposition did not have a significant impact on the stability of the modes, as the same modes are observed before and after ECCD channel 4 is turned on.

In the co-ECCD discharge, two regimes with regard to mode stability are clearly observed. When only the outermost ECCD channels are active, the low frequency modes are suppressed, while the high frequency modes are unstable. Then, as ECCD channel 4 is powered, with a current deposition location close to the axis at $s \approx 0.2$, all modes are suppressed. The location of current deposition seems to have a significant impact on mode stability in the co-ECCD discharge, in particular to the high frequency TAE. Drive and damping estimations are in agreement with the observed mode suppression regimes.

The single, most impactful effect of ECCD on TAE suppression is through the drive from the fast H population. Both counter-ECCD and co-ECCD contribute to decrease in the drive of the high frequency mode. In the case of the low frequency mode, drive decreases when co-ECCD is applied, which coincides with suppression of the modes, and slightly



increases when counter-ECCD is applied and the modes are observed in the discharge. The changes in drive are related to the radial position of the modes. When ECCD is applied, either co-ECCD or counter-ECCD, the high frequency modes are pushed outwards to regions of lower fast H temperature and weaker radial gradient, and drive decreases. In the case of the low frequency modes, counter-ECCD moves the mode inwards and drive increases, while co-ECCD moves the mode outwards and drive decreases. The effect of ECCD on damping also has a significant impact on the stability of the modes, particularly continuum damping. This damping source increases for both modes when ECCD is applied, either counter-ECCD or co-ECCD. This is due to changes in the continuum structure, either by partial closing of the TAE gap or by moving the surface where continuum damping occurs to locations of higher mode amplitude. Radiative damping follows the trend of increasing when modes are suppressed and decreasing when they are unstable, except for the high frequency mode during the co-ECCD discharge. A final word is directed to the impact of the ECCD deposition location. TAE activity changes after powering of channel 4, which affects the current profile at a different location than the other channels. The difference is most clear in the co-ECCD discharge where after this channel is turned on the previously unstable modes are suppressed.

Acknowledgments

This work has been carried out within the framework of the EUROfusion Consortium, funded by the European Union via the Euratom Research and Training Programme (Grant Agreement No. 101052200—EUROfusion). Views and opinions expressed are however those of the author(s) only and do not necessarily reflect those of the European Union or the European Commission. Neither the European Union nor the European Commission can be held responsible for them. The work of R Calado has been funded by the Fundação para a Ciência e a Tecnologia (FCT, Lisboa) under Grant No. PD/BD/142967/2018 and carried out as part of his training in the framework of the Advanced Program in Plasma Science and Engineering (APPLAuSE, sponsored by FCT under Grant No. PD/00505/2012) at Instituto Superior Técnico (IST). This work has also been funded by FCT under Project No. UIDB/04561/2020. IST activities also received financial support from Fundação para a Ciência e Tecnologia through Projects UIDB/50010/2020 and UIDP/50010/2020. The views and opinions expressed herein do not necessarily reflect those of FCT, of IST, or of their services.

ORCID iDs

R. Calado  <https://orcid.org/0000-0002-7716-2230>
 F. Nabais  <https://orcid.org/0000-0003-4644-2827>
 S.E. Sharapov  <https://orcid.org/0000-0001-7006-4876>
 P. Schneider  <https://orcid.org/0000-0001-7257-3412>
 Ye. Kazakov  <https://orcid.org/0000-0001-6316-5441>
 M. Garcia-Muñoz  <https://orcid.org/0000-0002-3241-502X>

A. Snicker  <https://orcid.org/0000-0001-9604-9666>
 J. Ferreira  <https://orcid.org/0000-0001-5015-7207>
 J. Galdon-Quiroga  <https://orcid.org/0000-0002-7415-1894>
 J. Gonzalez-Martin  <https://orcid.org/0000-0002-3237-5195>
 J. Stober  <https://orcid.org/0000-0002-5150-9224>
 G. Tardini  <https://orcid.org/0009-0002-0544-6880>
 M.A. Van Zeeland  <https://orcid.org/0000-0002-7911-2739>

References

- [1] Perkins F.W. *et al* 1999 *Nucl. Fusion* **39** 2137–74
- [2] Fasoli A. *et al* 2007 Progress in the ITER Physics Basis Chapter 5: Physics of energetic ions *Nucl. Fusion* **47** S264
- [3] Sharapov S.E. *et al* 2008 *Fusion Sci. Technol.* **53** 989–1022
- [4] Poedts S. and Kerner W. 1991 Ideal quasimodes reviewed in resistive magnetohydrodynamics *Phys. Rev. Lett.* **66** 2871
- [5] Poedts S., Kerner W., Goedbloed J.P., Keegan B., Huysmans G.T.A. and Schwarz E. 1992 Damping of global Alfvén waves in tokamaks due to resonant absorption *Plasma Phys. Control. Fusion* **34** 1397
- [6] Cheng C.Z., Chen L. and Chance M.S. 1985 High- n ideal and resistive shear Alfvén waves in tokamaks *Ann. Phys., NY* **161** 21–47
- [7] Fu G.Y. and Van Dam J.W. 1989 Excitation of the toroidicity-induced shear Alfvén eigenmode by fusion alpha particles in an ignited tokamak *Phys. Fluids B* **1** 1949
- [8] White R.B. and Chance M.S. 1984 Hamiltonian guiding center drift orbit calculation for plasmas of arbitrary cross section *Phys. Fluids* **27** 2455
- [9] Sigmar D.J., Hsu C.T., White R. and Cheng C.Z. 1992 Alpha-particle losses from toroidicity-induced Alfvén eigenmodes. Part II: Monte Carlo simulations and anomalous alpha-loss processes *Phys. Fluids B* **4** 1506
- [10] Van Zeeland M.A. *et al* 2008 Reversed shear Alfvén eigenmode stabilization by localized electron cyclotron heating *Plasma Phys. Control. Fusion* **50** 035009
- [11] Sharapov S.E. *et al* 2018 The effects of electron cyclotron heating and current drive on toroidal Alfvén eigenmodes in tokamak plasmas *Plasma Phys. Control. Fusion* **60** 014026
- [12] Garcia-Munoz M. *et al* 2019 Active control of Alfvén eigenmodes in magnetically confined toroidal plasmas *Plasma Phys. Control. Fusion* **61** 054007
- [13] Meyer H. *et al* 2019 Overview of physics studies on ASDEX Upgrade *Nucl. Fusion* **59** 112014
- [14] Sharapov S.E. *et al* 2020 Experiment on ECCD stabilisation of TAEs in AUG
- [15] Coster D.P., Basiuk V., Pereverzev G., Kalupin D., Zagórski R., Stankiewicz R., Huynh P. and Imbeaux F. 2010 The European transport solver *IEEE Trans. Plasma Sci.* **38** 2085–92
- [16] Kalupin D. *et al* 2011 Verification and validation of the European transport solver *38th EPS Conf. on Plasma Physics 2011 (EPS 2011—Europhysics Conf. Abstracts)* vol 35 pp 1348–51
- [17] Huysmans G.T.A., Goedbloed J.P. and Kerner W. 1991 *Proc. CP90 Conf. on Computational Physics (Amsterdam)* (World Scientific) p 371
- [18] Poedts S. and Schwartz E. 1993 Computation of the ideal-MHD continuous spectrum in axisymmetric plasmas *J. Comput. Phys.* **105** 165–8
- [19] Kerner W., Goedbloed J.P., Huysmans G.T.A., Poedts S. and Schwarz E. 1998 CASTOR: normal-mode analysis of resistive MHD plasmas *J. Comput. Phys.* **142** 271–303
- [20] Borba D. and Kerner W. 1999 *J. Comput. Phys.* **153** 101–38

- [21] Eriksson L.-G., Hellsten T. and Willen U. 1993 Comparison of time dependent simulations with experiments in ion cyclotron heated plasmas *Nucl. Fusion* **33** 1037
- [22] Rodrigues P., Figueiredo A., Ferreira J., Coelho R., Nabais F., Borba D., Loureiro N.F., Oliver H.J.C. and Sharapov S.E. 2015 Systematic linear-stability assessment of Alfvén eigenmodes in the presence of fusion α -particles for ITER-like equilibria *Nucl. Fusion* **55** 083003
- [23] Figueiredo A.C.A. *et al* 2016 Comprehensive evaluation of the linear stability of Alfvén eigenmodes driven by alpha particles in an ITER baseline scenario *Nucl. Fusion* **56** 076007